**IEEE Robotics and Automation Letters (RAL) paper presented at the**
**2020 IEEE/RSJ International Conference on Intelligent Robots and Systems (IROS)**
**October 25-29, 2020, Las Vegas, NV, USA (Virtual)**

# Incomplete Orientation Mapping for Teleoperation with One DoF Master-Slave Asymmetry

Gaofeng Li, Fernando Caponetto, Edoardo Del Bianco,
Vasiliki Katsageorgiou, Ioannis Sarakoglou, and Nikos G. Tsagarakis

***Abstract*— Teleoperation systems require a human-centered approach in which the kinematic mapping is intuitive and straightforward for the operators. However, a mismatch in the degrees-of-freedom (DoFs) between master and slave could result in an asymmetrical teleoperation system. That is an obstacle for intuitive kinematic mapping. In particular, it is even more challenging when the missing DoF is a pure rotational DoF, since the rotation group $SO(3)$ is a nonlinear Riemannian manifold. This paper is concerned with an asymmetric teleoperation system, where the master subsystem can provide 6-DoF pose sensing while the slave subsystem only has 5 DoFs. The rotation along the missing DoF, which is configuration-dependent, is mapped to a geodesic curve in $SO(3)$. We define and prove the closed-form solution of the perpendicular curve to the geodesic curve. Based on the perpendicular curve, we develop a novel Incomplete Orientation Mapping (IOM) approach to avoid the motion in the missing DoF. By comparing with two baseline methods, the experimental results demonstrate that the proposed method can discard the rotational motion along the missing DoF for all configurations, while preserving the remaining rotations.**

## I. Introduction

Teleoperation systems have found numerous applications [1], [2] in search and rescue [3], space [4], and robot-assisted medical intervention [5]. Performing a task through teleoperation allows operators to keep a safe distance from a dangerous environment as well as to take advantage of the robots' capabilities in higher power, higher precision, etc.. In order to provide an immersive experience to operators, intuitive kinematic mapping is a fundamental requirement for an effective teleoperation system.

Most of the relevant literature is focused on symmetric Single-Master/Single-Slave (SMSS) systems [6], [7], in which the master and slave subsystems have the same number of robots and the same degrees-of-freedom (DoFs). However, considering the increasing complexity of teleoperation tasks and the diversity of master/slave devices, the mismatch in the DoFs, and/or the number of master and slave devices is ubiquitous.

Manuscript received February 23, 2020; Revised May 20, 2020; Accepted June 19, 2020.

This paper was recommended for publication by Editor Allison Okamura upon evaluation of the Associate Editor and Reviewers' comments.

This research is funded by the Italian National Institute for Insurance against Workplace Accidents (INAIL)

The authors are with the Humanoids and Human Centered Mechatronics research line of Istituto Italiano Di Technologia (IIT), Via Morego 30, 16163, Genova, Italy. (e-mails: gaofeng.li@iit.it, fernando.caponetto@iit.it, edoardo.delBianco@iit.it, vasiliki.katsageorgiou@iit.it, ioannis.sarakoglou@iit.it, nikos.tsagarakis@iit.it). Ioannis Sarakoglou is the corresponding author.

Digital Object Identifier (DOI): see top of this page.

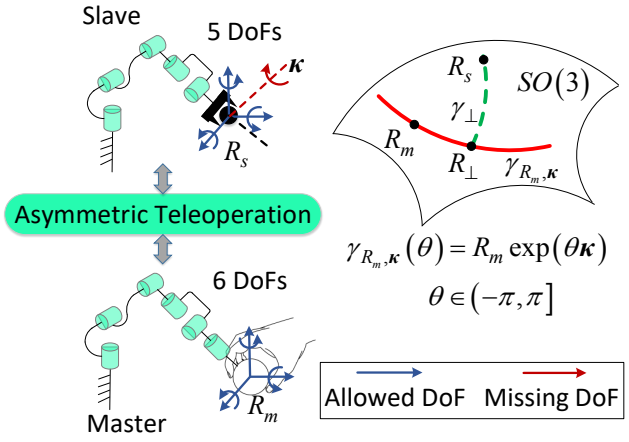


Fig. 1. The asymmetric teleoperation system where the master/slave have different DoFs. Due to the deficiency in DoF, the slave robot loses the rotation ability along $\boldsymbol{\kappa}$. The locus of $R_m$ (the rotation matrix of the master device) rotating around $\boldsymbol{\kappa}$ forms a geodesic curve $\gamma_{R_m,\boldsymbol{\kappa}}(\theta)$ in $SO(3)$. We define and prove the closed-form solution of the perpendicular curve $\gamma_\perp$, which is the shortest path from $R_s$ (The current rotation matrix of the slave robot) to $R_m$. By decomposing the rotation into two orthogonal subspaces: the one along $\gamma_{R_m,\boldsymbol{\kappa}}(\theta)$ and the other one along $\gamma_\perp$, we can only discard the rotational motion along $\gamma_{R_m,\boldsymbol{\kappa}}(\theta)$, while preserving the remaining rotations.

Significant research has been conducted on the subject of asymmetric teleoperation systems. Most of the research efforts have been focused on asymmetric teleoperation architectures involving Multiple-Master/Multiple-Slave (MMMS) systems, where the master and slave have different number of agents. Malysz *et al.* [8] have summarized several important examples that depart from conventional symmetric SMSS systems: 1) Multiple-Master/Single-Slave (MMSS) control of a Kinematically Redundant Slave Robot (KRSR) [9]–[13]. In this example, the first master device is designated to control a primary task control frame; meanwhile, another master device can manipulate a secondary task frame attached to the KRSR. 2) Single-Master/Multiple-Slave (SMMS) control of a twin-armed slave system [14]–[17]. In this example, the multiple slave robots can be controlled autonomously for formation and/or grasping. The single master device is teleoperated to control the average position of the slave end-effectors or control a frame representing the slave robots formation. 3) Single-Master control of a Kinematically Deficient Slave Robot (KDSR) [11], [18], [19], which is similar but still different to our problem. In this example, the slave robot is a kinematically deficient mobile robot subjected to a nonholonomic constraint such that it has only two

control motions to position itself in a 3-D planar space. An asymmetrical teleoperation system results when a 3DoF master device is used.

Another group of asymmetric teleoperation systems are the tele-manipulation systems in which the hand exoskeleton is used as the master device and the robotic hand is used as the slave robot [20], [21]. Considering the ability to manipulate objects with diverse shapes and sizes, the robotic hand may be chosen to be anything from a highly anthropomorphic dexterous hand [22], [23] to a simpler industrial gripper [24]. The diversity of the robotic hands [25], [26] in kinematics, sensing, and actuation, and their typical differences to the commanding human hand, result in significant asymmetries to the master-slave system. To address such asymmetries, Brygo *et al.* [27], [28] proposed a Cartesian-based hand synergy matrix to map the exoskeleton's fingertip Cartesian trajectory to the degree of closure of the Pisa/IIT SoftHand, serving as the slave robot. Conversely, the interaction force estimated at the robotic hand as a 1-DoF grasping torque can be inversely mapped to a 9-D reference in the fingertips Cartesian space through an inverse projection of the Cartesian-based synergy matrix. Salvietti *et al.* [29] noticed that the dissimilar kinematic structure in master and slave devices may lead to a different number of interaction points on the master side and of contact points in the slave side, and they accordingly proposed a new forward and backward mapping algorithm to address this scenario.

This paper is concerned with an asymmetrical teleoperation system, where the master device can provide 6-DoF pose sensing while the slave robot only has 5 DoFs. It is a common situation that the slave robot has dissimilar kinematic structure to the master device. This can have the effect that the reachable poses in the master's workspace cannot be directly mapped to and reproduced by the commanded slave, in its workspace. In the master-slave setup implemented in this paper and shown in Fig. 1, the slave robot loses the rotation ability along a specific direction, which is referred to as the missing DoF in the following part of this paper. When there is a 6-DoF pose sensing input from the master side, the motion along the available DoFs should be mapped to the slave to provide intuitive and straightforward mapping. While the sensed motion along the missing DoF should be avoided to guarantee safety, since the unreachable input to the slave controller may lead to unstable behaviors. However, how to decompose the 6-DoF pose into two orthogonal subspaces is challenging. In particular, it is even more challenging when the missing DoF is a pure rotation, since the rotation group $SO\,(3)$ is a nonlinear Riemannian manifold.

The rotation along the missing rotational DoF is mapped to a geodesic curve in $SO\,(3)$. In this paper, we define and prove the closed-form solution of the perpendicular curve to the geodesic curve. By decomposing the rotation into the two orthogonal subspaces: one along the geodesic curve and another one along its perpendicular curve, we develop a novel perpendicular curve-based Incomplete Orientation Mapping (IOM) approach to find a reachable orientation in the geodesic curve and avoid the motion along the missing DoF. The experiments demonstrate that the proposed method can prevent unreachable orientation references to the slave manipulator, while preserving the remaining rotations.

Another straightforward solution to the DoF asymmetry would be to lock the rotational motion along the missing DoF of the slave at the master device. However, this solution is limited to haptic teleoperation systems with substantially strong force feedback devices at the master side, capable of constraining the motion of the operator along the missing DoF of the slave. The action of the IOM approach is decoupled with the motion constraints provided by the force feedback action and provides an additional level of safety. The unintentional orientations, which are encountered at the master side along the missing DoF due to low stiffness or low force capacity of the haptic device (or no force feedback), can be always detected and corrected by the proposed method. Therefore, these assistive/guidance actions can be modulated to any desirable level of haptic impedance within the performance capabilities of the master device.

The rest of this paper is organized as follows. Section II gives the problem statement. Section III reviews the basic concepts and notations regarding the rotation group $SO\,(3)$. Section IV defines the perpendicular curve in $SO\,(3)$ and proves its closed-form solution. Section V presents the proposed perpendicular curve-based IOM approach. Section VI gives the experimental results to validate the proposed method. The conclusion and future work are finally summarized in Section VII.

## II. Problem Statement

Consider a SMSS teleoperation system with DoF asymmery. For the sake of convenience, the following notations are defined:

- $\boldsymbol{p}_m$, $R_m$: The position and orientation sensed by the master device.
- $\boldsymbol{p}_s$, $R_s$: The current position and orientation of the slave robot.
- $\boldsymbol{p}_{sd}$, $R_{sd}$: The desired position and orientation for the slave robot.
- $\boldsymbol{\kappa}$: The direction of the missing DoF. Without loss of generality, $\boldsymbol{\kappa}$ is chosen as a unit vector. According to the kinematic structure of the slave robot, $\boldsymbol{\kappa}$ is configuration-dependent. Here we assume that $\boldsymbol{\kappa}$ can be calculated according to the slave robot's configuration.

As shown in Fig. 2, the forward kinematic mapping problem with DoF asymmetry is defined as:

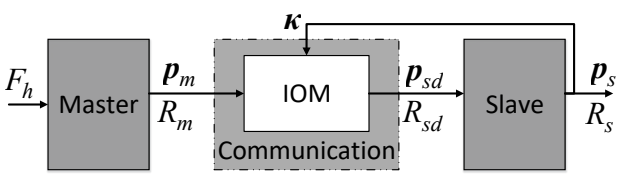


Fig. 2. The IOM problem for teleoperation system with DoF asymmetry.

*Definition 1 (**Incomplete Orientation Mapping (IOM) Problem**):* Given $\boldsymbol{p}_m$, $R_m$, $\boldsymbol{p}_s$, $R_s$, and $\boldsymbol{\kappa}$, determine a desired position $\boldsymbol{p}_{sd}$ and orientation $R_{sd}$ for the slave robot such that $\boldsymbol{p}_{sd}, R_{sd}$ is reachable by the slave robot and only the motion along $\boldsymbol{\kappa}$ is avoided.

## III. Mathematic Preliminaries

This section reviews the basic notations about the Angle-Axis Space and the geodesic in rotation group $SO(3)$. Readers may refer to [30], [31] and [32] for more details.

### A. The Angle-Axis Space

Every orientation $R \in SO(3)$ can be represented as a rotation of an angle about an axis by at most $\pi$ radians. Define a closed ball $B_\pi$ of radius $\pi$ in $\mathbb{R}^3$ as:

$$B_\pi = \left\{ \boldsymbol{\omega} \in \mathbb{R}^3 \,|\, \|\boldsymbol{\omega}\| \leq \pi \right\}. \tag{1}$$

Consequently, any orientation $R \in SO(3)$ can be represented by a vector $\boldsymbol{\omega} \in B_\pi$, in which the direction of $\boldsymbol{\omega}$ is the axis and the norm $\|\boldsymbol{\omega}\|$ is the angle.

However, as well known, the mapping from $B_\pi$ to $SO(3)$ is one-to-one in the interior and two-to-one on the boundary of the ball. To avoid ambiguity, a half sphere $S^2$ in $\mathbb{R}^3$ is defined:

$$S^2 = \left\{ \boldsymbol{\omega} \in \mathbb{R}^3 \,|\, \|\boldsymbol{\omega}\| = \pi \text{ and } (q_1 \text{ or } q_2 \text{ or } q_3) \right\}, \tag{2}$$

where conditions $q_1$, $q_2$, and $q_3$ are defined as following:

$$\begin{aligned} q_1: &\quad \omega_x < 0, \\ q_2: &\quad \omega_x = 0 \quad \text{and} \quad \omega_y < 0, \\ q_3: &\quad \omega_x = 0 \quad \text{and} \quad \omega_y = 0 \quad \text{and} \quad \omega_z < 0, \end{aligned} \tag{3}$$

where $\omega_x$, $\omega_y$, and $\omega_z$ are the entries of $\boldsymbol{\omega}$.

Thus, $SO(3)$ is bijective to $B_\pi \backslash S^2$, where $U \backslash A$ is the relative complement set of $A$ in $U$. $B_\pi \backslash S^2$ is called Angle-Axis Space. The mappings between $SO(3)$ and $B_\pi \backslash S^2$ can be given by the exponential mapping $\exp(\boldsymbol{\omega})$ and the logarithm mapping $\log(R)$ as introduced in [32].

### B. The Distance Metric and Geodesic in $SO(3)$

*Definition 2:* The distance between two orientations $R_1$ and $R_2$ is defined as the angle of the rotation $R_1^T R_2$:

$$d_\angle(R_1, R_2) = \left\| \log\left(R_1^T R_2\right) \right\|. \tag{4}$$

*Proposition 1:* For any orientations $R \in SO(3)$, $R_1 \in SO(3)$, $R_2 \in SO(3)$, the following equation is always true:

$$d_\angle(RR_1, RR_2) = d_\angle(R_1, R_2) \tag{5}$$

*Proposition 2:* For any two orientations $R_1 \in SO(3)$, $R_2 \in SO(3)$, the following equation is always true:

$$d_\angle(R_1, R_2) = \arccos\left(\frac{tr\left(R_1^T R_2\right) - 1}{2}\right). \tag{6}$$

*Proposition 3:* The geodesic curve in $SO(3)$ from $R_1$ to $R_2$ is given by:

$$\gamma(\zeta) = R_1 \exp\left(\zeta \log\left(R_1^T R_2\right)\right) \qquad \zeta \in [0, 1], \tag{7}$$

which is a one-parameter family of orientations.

Given an orientation $R_m$ and a unit vector $\boldsymbol{\kappa}$, a one-parameter family of orientations can be obtained by rotating about $\boldsymbol{\kappa}$ by an angle $\theta$:

$$\gamma_{R_m,\boldsymbol{\kappa}}(\theta) = R_m \exp(\theta \boldsymbol{\kappa}), \tag{8}$$

where $\theta \in (-\pi, \pi]$ is the varying parameter. $\gamma_{R_m,\boldsymbol{\kappa}}(\theta)$ is a geodesic curve in $SO(3)$.

*Definition 3:* For any orientation $R_s \in SO(3)$, we define the geodesic distance from $R_s$ to a curve $\gamma_{R_m,\boldsymbol{\kappa}}(\theta)$ as:

$$d_\angle(R_s, \gamma_{R_m,\boldsymbol{\kappa}}(\theta)) = \min_{\theta \in (-\pi,\pi]} d_\angle(R_s, R_m \exp(\theta \boldsymbol{\kappa})). \tag{9}$$

*Definition 4:* We define the foot-of-perpendicular (FOP) from $R_s \in SO(3)$ to a curve $\gamma_{R_m,\boldsymbol{\kappa}}(\theta)$ as:

$$R_\perp = R_m \exp(\theta_{\min} \boldsymbol{\kappa}), \tag{10}$$

where

$$\theta_{\min} = \arg \min_{\theta \in (-\pi,\pi]} d_\angle(R_s, R_m \exp(\theta \boldsymbol{\kappa})). \tag{11}$$

*Definition 5:* We define the perpendicular curve from $R_s \in SO(3)$ to a curve $\gamma_{R_m,\boldsymbol{\kappa}}(\theta)$ as:

$$\gamma_\perp(\zeta) = R_s \exp\left(\zeta \log\left(R_s^T R_\perp\right)\right) \quad \zeta \in [0, 1], \tag{12}$$

which is the geodesic curve from $R_s$ to $R_\perp$.

*Lemma 1:* Given any orientation $R_s \in SO(3)$ and a curve $\gamma_{R_m,\boldsymbol{\kappa}}(\theta)$, the FOP $R_\perp$ is given by:

$$R_\perp = \begin{cases} R_s \exp\left(\frac{1}{2}\overline{\boldsymbol{\omega}}\right), & \text{if } \log(\mathrm{R_c}) \times \boldsymbol{\kappa} = \mathbf{0}, \\ R_s \exp\left(-\frac{2\pi - \|\overline{\boldsymbol{\omega}}\|}{2\|\overline{\boldsymbol{\omega}}\|}\overline{\boldsymbol{\omega}}\right), & \text{otherwise}, \end{cases} \tag{13}$$

where "$\times$" is the cross product of two vectors, and

$$\boldsymbol{\omega}_1 = \log\left(R_m^T R_s\right), \tag{14}$$

$$\boldsymbol{\omega}_2 = 2\boldsymbol{\kappa}^T \boldsymbol{\omega}_1 \boldsymbol{\kappa} - \boldsymbol{\omega}_1, \tag{15}$$

$$\overline{\boldsymbol{\omega}} = \log\left(\exp^T(\boldsymbol{\omega}_1) \exp(\boldsymbol{\omega}_2)\right), \tag{16}$$

$$R_c = \exp(\boldsymbol{\omega}_1) \exp\left(\frac{1}{2}\overline{\boldsymbol{\omega}}\right). \tag{17}$$

*Proof:* For any $\theta \in (-\pi, \pi]$, we have:

$$\begin{aligned} d_\angle(R_s, R_m \exp(\theta \boldsymbol{\kappa})) &= d_\angle\left(R_m^T R_s, \exp(\theta \boldsymbol{\kappa})\right) \\ &= d_\angle(\exp(\boldsymbol{\omega}_1), \exp(\theta \boldsymbol{\kappa})). \end{aligned} \tag{18}$$

Therefore, the distance from $R_s$ to the curve $\gamma_{R_m,\boldsymbol{\kappa}}(\theta)$ is equal to the distance from $\exp(\boldsymbol{\omega}_1)$ to the curve $\gamma_{I,\boldsymbol{\kappa}}(\theta)$.

$\theta\boldsymbol{\kappa}$ gives a diameter of $B_\pi$ in the Angle-Axis Space whose direction is determined by $\boldsymbol{\kappa}$. Obviously, $\boldsymbol{\omega}_1$ and $\boldsymbol{\omega}_2$ are symmetrical about $\theta\boldsymbol{\kappa}$. The following properties can be easily verified:

$$\|\boldsymbol{\kappa}\| = 1, \tag{19}$$

$$\|\boldsymbol{\omega}_1\| = \|\boldsymbol{\omega}_2\|. \tag{20}$$

Then we have:

$$\begin{aligned} &d_\angle(\exp(\boldsymbol{\omega}_i), \exp(\theta \boldsymbol{\kappa})) \\ &\quad = \arccos\left(\frac{tr\left(\exp^T(\boldsymbol{\omega}_i) \exp(\theta \boldsymbol{\kappa})\right) - 1}{2}\right), \end{aligned} \tag{21}$$

where $i = 1, 2$. It is easy to verify that (See Appendix):

$$tr\left(\exp^T(\boldsymbol{\omega}_1)\exp(\theta\boldsymbol{\kappa})\right) = tr\left(\exp^T(\boldsymbol{\omega}_2)\exp(\theta\boldsymbol{\kappa})\right). \quad (22)$$

Thus,

$$d_{\angle}(\exp(\boldsymbol{\omega}_1), \exp(\theta\boldsymbol{\kappa})) = d_{\angle}(\exp(\boldsymbol{\omega}_2), \exp(\theta\boldsymbol{\kappa})) \quad (23)$$

The foot of perpendicular from $\exp(\boldsymbol{\omega}_1)$ to the curve $\gamma_{I,\boldsymbol{\kappa}}(\theta)$, $\overline{R}_{\perp}$, must be at the midpoint of the smaller geodesic arc from $\exp(\boldsymbol{\omega}_1)$ to $\exp(\boldsymbol{\omega}_2)$ when $d_{\angle}\left(\exp(\boldsymbol{\omega}_1), \overline{R}_{\perp}\right) \leq \frac{\pi}{2}$ or the midpoint of the longer geodesic arc from $\exp(\boldsymbol{\omega}_1)$ to $\exp(\boldsymbol{\omega}_2)$ when $d_{\angle}\left(\exp(\boldsymbol{\omega}_1), \overline{R}_{\perp}\right) > \frac{\pi}{2}$:

$$\overline{R}_{\perp} = \begin{cases} R_c, & \text{if} \quad \log(\mathrm{R_c}) \times \boldsymbol{\kappa} = \mathbf{0}, \\ \exp(\boldsymbol{\omega}_1)\exp\left(-\frac{2\pi - \|\overline{\boldsymbol{\omega}}\|}{2\|\overline{\boldsymbol{\omega}}\|}\overline{\boldsymbol{\omega}}\right), & \text{else.} \end{cases} \quad (24)$$

Thus,

$$R_{\perp} = R_m \overline{R}_{\perp} = \begin{cases} R_s \exp\left(\frac{1}{2}\overline{\boldsymbol{\omega}}\right), & \text{if} \quad \log(\mathrm{R_c}) \times \boldsymbol{\kappa} = \mathbf{0}, \\ R_s \exp\left(-\frac{2\pi - \|\overline{\boldsymbol{\omega}}\|}{2\|\overline{\boldsymbol{\omega}}\|}\overline{\boldsymbol{\omega}}\right), & \text{else.} \end{cases} \quad (25)$$

The proof is complete. ■

*Corollary 1.1:* The perpendicular curve $\gamma_{\perp}(\zeta)$ is given by

$$\gamma_{\perp}(\zeta) = R_s \exp\left(\zeta R_s^T R_{\perp}\right) \quad \zeta \in [0, 1]. \quad (26)$$

*Corollary 1.2:* $\gamma_{\perp}(\zeta)$ gives the shortest path from $R_s$ to the curve $\gamma_{R_m,\boldsymbol{\kappa}}(\theta)$ in $SO(3)$.

## V. The Incomplete Orientation Mapping (IOM) Algorithm in Case Study

To better demonstrate the proposed perpendicular curve-based Incomplete Orientation Mapping (IOM) algorithm, we take the asymmetric teleoperation system, where the master subsystem can provide 6-DoF pose sensing and the slave subsystem has only 5 DoFs, as an example.

The configuration of the slave manipulator, which is named Teleop-Man, is shown in Fig. 3. To simplify the problem, the controlled frame of the slave robot is placed on the wrist of the Teleop-Man. The first three joints of the slave robot determine the position and the last two joints determine the orientation. Due to the deficiency in DoF, the slave robot loses the rotation ability around the direction $\boldsymbol{\kappa}$, which is perpendicular to the axes of the 4-th and 5-th joints. The robotic hand, which is installed on the end-effector of the Teleop-Man, is controlled by a hand exoskeleton. In this paper, the teleoperation of the robotic hand is not involved.

Please note that the missing DoF $\boldsymbol{\kappa}$ is a unit vector and is expressed in the wrist's frame. According to the geometric relationship, we can have:

$$\boldsymbol{\kappa} = [\cos(q_5), 0, -\sin(q_5)]^T, \quad (27)$$

where $q_5$ is the joint value of the 5-th joint. As stated before, $\boldsymbol{\kappa}$ is configuration-dependent.

Since the missing DoF $\boldsymbol{\kappa}$ is a pure rotational DoF, the position of the master device can be directly mapped to the slave robot:

$$\boldsymbol{p}_{sd} = \boldsymbol{p}_m. \quad (28)$$

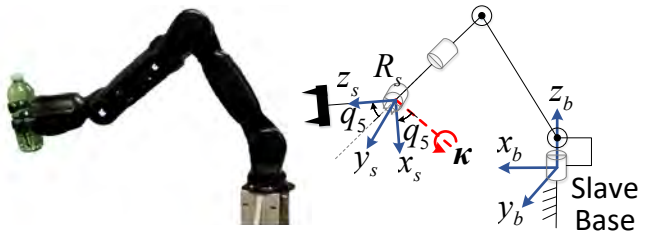


Fig. 3. The configuration of the 5-DoF slave manipulator, which is named Teleop-Man. To simplify the problem, the controlled frame is chosen as the wrist of the Teleop-Man. In this case, the position is only determined by the first three joints and the orientation is only determined by the last two joints. The missing DoF is a pure rotational DoF.

As presented in Section IV, the locus of $R_m$, which is the rotation matrix of the master device, forms a geodesic curve $\gamma_{R_m,\boldsymbol{\kappa}}(\theta)$ by rotating around $\boldsymbol{\kappa}$. Based on the perpendicular curve, the proposed IOM algorithm is to map the orientation of the master device to the FOP $R_{\perp}$:

$$R_{sd} = R_{\perp} = \begin{cases} R_s \exp\left(\frac{1}{2}\overline{\boldsymbol{\omega}}\right), & \text{if} \quad \log(\mathrm{R_c}) \times \boldsymbol{\kappa} = \mathbf{0}, \\ R_s \exp\left(-\frac{2\pi - \|\overline{\boldsymbol{\omega}}\|}{2\|\overline{\boldsymbol{\omega}}\|}\overline{\boldsymbol{\omega}}\right), & \text{else,} \end{cases} \quad (29)$$

where $\overline{\boldsymbol{\omega}}$ and $R_c$ are given by **Lemma 1**.

The geodesic curve $\gamma_{R_m,\boldsymbol{\kappa}}(\theta)$ in a Riemannian manifold is analogous to the straight line in Euclidean space. Accordingly, the shortest path $\gamma_{\perp}(\zeta)$ in a Riemannian manifold is analogous to the perpendicular line of the straight line in Euclidean space. This is where the terminology "Perpendicular Curve" comes from. As shown in Fig. 4, the orientation $R_m$ sensed by the master device gives the desired goal orientation for the slave robot. However, due to the deficiency in DoF, the slave robot loses the rotation ability around the direction $\boldsymbol{\kappa}$. Similarly to the perpendicular line in Euclidean space, the rotation can be decomposed into two orthogonal subspaces: the one along the geodesic curve $\gamma_{R_m,\boldsymbol{\kappa}}(\theta)$ and the other one along its perpendicular curve $\gamma_{\perp}$. By mapping $R_m$ to $R_{\perp}$, the rotational motion along $\gamma_{R_m,\boldsymbol{\kappa}}(\theta)$ is discarded. Only the rotation along $\gamma_{\perp}$ is preserved. Since the proposed mapping algorithm discards the rotational part along the missing DoF $\boldsymbol{\kappa}$, it is named by Incomplete Orientation Mapping (IOM) algorithm.

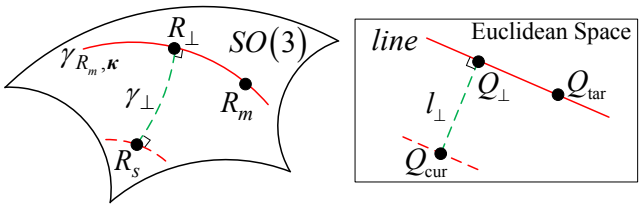


Fig. 4. The geodesic curve and its perpendicular curve can be analogous to the straight line and its perpendicular line in Euclidean space. Similar to the Euclidean space, the rotation can also be decomposed into two directions: one is along itself and the other one is along its perpendicular line.

## VI. Experiments

To validate the feasibility and effectiveness of the proposed IOM algorithm, two groups of experiments are carried out. In the first group, the Directly Mapping Method (DMM, the position and orientation of the master device is directly mapped to the slave manipulator without any operation) is chosen as a baseline comparison to validate the effectiveness of the proposed IOM algorithm. In the second group, 2 different mapping strategies are chosen as comparisons to validate the advantages of the IOM algorithm.

### A. Experimental Setup

As shown in Fig. 5, the Haption Virtuose 6D serves as the grounded master device to provide 6-DoF pose sensing. The 5-DoF Teleop-Man, which serves as the slave manipulator, works in Cartesian position control mode and accepts the desired 6-DoF pose as input. The pose of the end-effector is calculated according to the forward kinematics by the slave controller. Due to the deficiency in DoF, the slave controller formulates the control problem as a two-layer optimization problem in which the position is chosen as the primary objective and the orientation is chosen as the secondary objective. The position $\boldsymbol{p}_m$ and orientation $R_m$ sensed by the master device are sent to the teleoperation master software (named ToM) running on the master station computer. Our IOM algorithm is embedded into ToM. The communication loop between master-ToM and ToM-slave are both set to be 1kHz. To better focus on the DoF asymmetry, the time delay is ignored.

The visual information regarding the slave manipulator is fed to the human operator in the master station. To provide more intuitive visual feedback, the initial bias between the master and the slave device has been compensated by:

$$\begin{aligned} \boldsymbol{p}_m &= {}^o R_m \boldsymbol{p}_{m(t)} + \left(\boldsymbol{p}_{s_0} - {}^o R_m \boldsymbol{p}_{m_0}\right), \\ R_m &= \left({}^o R_m R_{m(t)}\right) \left(\left({}^o R_m R_{m_0}\right)^T R_{s_0}\right), \end{aligned} \tag{30}$$

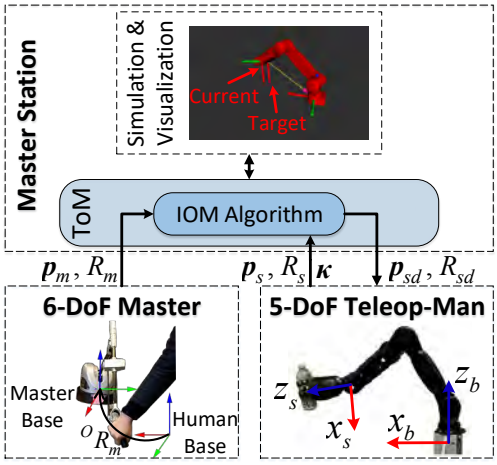


Fig. 5. The experimental setup. The master device can provide 6-DoF pose sensing and the slave robot only has 5 DoFs. The goal of the proposed IOM algorithm, which is embedded into ToM, is to find a reachable target pose reference and send it to the slave manipulator.

where ${}^o R_m$ is the rotation matrix of the master's base frame relative to the human operator's base frame, $\boldsymbol{p}_{m_0}$ and $R_{m_0}$ are the initial position and orientation sensed by the master and relative to the master's base frame, $\boldsymbol{p}_{s_0}$ and $R_{s_0}$ are the initial position and orientation of the slave manipulator relative to the slave's base frame, $\boldsymbol{p}_{m(t)}$ and $R_{m(t)}$ are the current position and orientation readings of the master device.

In our system, the slave manipulator can be either a simulated one or a physical one. In order to guarantee safety, during the testing of the comparison methods (i.e. the DMM), the slave robot is implemented in simulation, since the comparison methods may map unreachable targets to the slave and lead to danger.

### B. Baseline Comparison: DMM

To better illustrate the effectiveness of the IOM method in rotational motion decomposition, the missing DoF $\boldsymbol{\kappa}$ is set to be the $x$-axis ($\boldsymbol{\kappa} = [1, 0, 0]^T$) so that the discarded rotational part is only on the $x$ component. The DMM is chosen as a baseline comparison.

For both methods, the human operator is asked to control the slave manipulator to move freely in the workspace. In particular, the slave manipulator's motion ability in all directions (3 translations and 3 rotations) are tested. During the movement, we try our best to keep the 5-th joint value $q_5$ to be zero since $\boldsymbol{\kappa}$ is set to be the $x$-axis in the tests. The trajectories of the master and slave are recorded in real-time. More details about the experiments are shown in the attached video.

Since the missing DoF is a pure rotational DoF, the DMM and the proposed IOM method share the same performance in terms of position error. The orientation errors between $R_s$

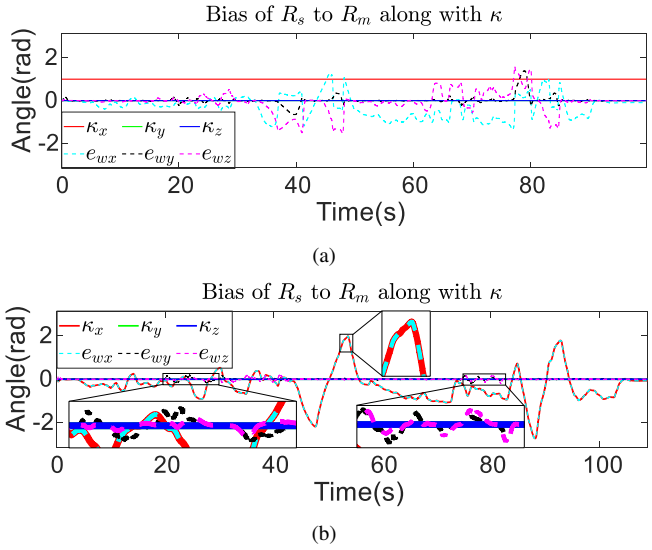


Fig. 6. The orientation error curves of the two methods: (a) The DMM. (b) The IOM method. The missing DoF $\boldsymbol{\kappa} = [1, 0, 0]^T$ is also presented in both figures and has been scaled in (b). As we can see, the IOM method only has big errors in $x$-axis, which is exactly the missing DoF direction $\boldsymbol{\kappa}$. In contrast, the DMM method leads to big errors in all directions.

and $R_m$ for the two methods are shown in Fig. 6. To better illustrate the effect of rotational motion decomposition, the direction $\boldsymbol{\kappa}$ is also presented. In particular, $\boldsymbol{\kappa}$ has been scaled in Fig. 6(b) by:

$$\overline{\boldsymbol{\kappa}} = sign * \left\| \log\left(R_m^T R_{sd}\right) \right\| * \boldsymbol{\kappa}, \tag{31}$$

where $sign = 1$ if $\log\left(R_m^T R_{sd}\right)$ has the same direction with $\boldsymbol{\kappa}$ and $sign = -1$ if they have the opposite direction.

As shown in Fig. 6(b), the scaled missing DoF direction $\overline{\boldsymbol{\kappa}}$ almost overlaps with the orientation error curve. This demonstrates that the IOM method can discard the rotational part along $\boldsymbol{\kappa}$ (the $x$-axis) and guarantee smaller errors in the other directions (the $y$- and $z$-axis). In contrast, the DMM method leads to big errors in all directions, which is not intuitive and straightforward for human operators.

The orientation errors between $R_s$ and $R_{sd}$ and the bias between $R_{sd}$ to $R_m$ of the IOM method are presented in Fig. 7(a) and Fig. 7(b), respectively. As shown in Fig. 7(a), the errors between $R_s$ and $R_{sd}$ are much smaller than those of the DMM method. This result demonstrates that the unreachable rotation along the missing DoF $\boldsymbol{\kappa}$ has been discarded and the mapping results $R_{sd}$ of the IOM algorithm are all reachable by the slave robot. As shown in Fig. 7(b), the scaled missing DoF direction $\overline{\boldsymbol{\kappa}}$ overlaps perfectly with the bias between $R_{sd}$ to $R_m$. This result validates that our mapping results only discard the rotational part along $\boldsymbol{\kappa}$.

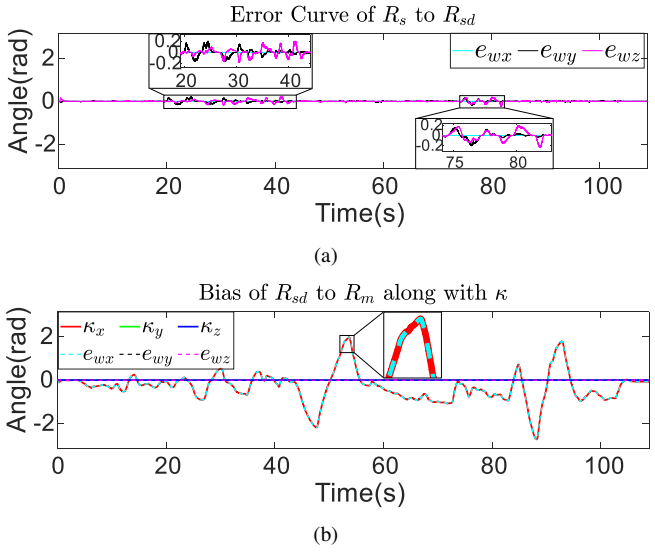


Fig. 7. The result of the IOM method. (a) The errors between $R_s$ and $R_{sd}$ are much smaller than those of the DMM method (see Fig. 6(a)). (b) The bias between $R_{sd}$ to $R_m$ along with $\boldsymbol{\kappa}$ ($\boldsymbol{\kappa}$ has been scaled). The overlapping of the bias with the scaled $\boldsymbol{\kappa}$ shown in (b) demonstrates that our mapping results only discard the rotational part along $\boldsymbol{\kappa}$.

### C. Comparison to 2 Different Mapping Strategies

In the first group of experiments, the effectiveness of the IOM method has been demonstrated by choosing a constant $\boldsymbol{\kappa}$. However, the missing DoF direction $\boldsymbol{\kappa}$ is configuration-dependent. To better demonstrate the advantages of the IOM method, 2 different mapping strategies have been carried out as comparisons in the second group of experiments. These methods were chosen from the state of the art as being the most applicable to our problem.

The first strategy is the DMM which serves as a baseline method. The second strategy (named EPDM, Excluding Predefined DoF Method), which is a borrowed idea from [33], is to predefine an 'unused' DoF and exclude the 'unused' component from the pose vector. Suppose we have $\boldsymbol{p}_m = [p_{mx}, p_{my}, p_{mz}]^T$, $R_m = \exp\left([\omega_{mx}, \omega_{my}, \omega_{mz}]^T\right)$, $R_s = \exp\left([\omega_{sx}, \omega_{sy}, \omega_{sz}]^T\right)$, and the predefined DoF is $x$-axis. Then the third mapping strategy is given by:

$$\begin{aligned} \boldsymbol{p}_{sd} &= \boldsymbol{p}_m = [p_{mx}, p_{my}, p_{mz}]^T \\ R_{sd} &= \exp\left([\omega_{sx}, \omega_{my}, \omega_{mz}]^T\right), \end{aligned} \tag{32}$$

where the $x$ component of the rotation is discarded directly.

For each method, the human operator is asked to test the rotational motion ability of the slave in three configurations. As shown in Fig. 8, the missing DoF direction $\boldsymbol{\kappa}$ expressed in the wrist frame varies with the configuration.

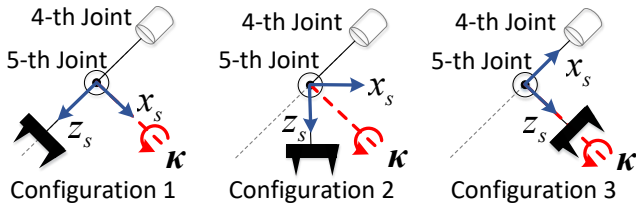


Fig. 8. The 3 configurations to test the rotational motion ability. The missing DoF direction $\boldsymbol{\kappa}$ is configuration-dependent.

As shown in Fig. 9(a)(b)(c), the DMM method fails to avoid the unreachable orientation mappings and leads to big errors for all the three configurations.

As shown in Fig. 9(d)(e)(f), the EPDM works well for the first configuration since the missing DoF $\boldsymbol{\kappa}$ is coincidentally aligned the predefined DoF. Moreover, the errors between $R_s$ and $R_{sd}$ are much smaller than those of the DMM for both the first and second configurations. This demonstrates that the EPDM can avoid the unreachable orientation mappings for these two cases. However, the EPDM fails for the third configuration, in which $\boldsymbol{\kappa}$ is perpendicular to the predefined DoF. This is a singularity configuration for the EPDM since $\boldsymbol{\kappa}$ has no component on the predefined DoF. Moreover, as shown in Fig. 9(d)(e), the bias between $R_{sd}$ and $R_m$ does not overlaps with the scaled $\boldsymbol{\kappa}$ for the second and third configurations. This means that the rotational part discarded by the EPDM is not only in the missing DoF. Therefore, the intuitiveness of the EPDM is jeopardised.

In contrast, the proposed method works well for all the three configurations. As shown in Fig. 9(g), the $e_{wx}$ (cyan) and $\kappa_x$ (red), the $e_{wy}$ (black) and $\kappa_y$ (green), and the $e_{wz}$ (magenta) and $\kappa_z$ (blue) are overlapped perfectly. The overlapping shown in Fig. 9(g)(h) demonstrates that our mapping results only discard the rotational part around $\boldsymbol{\kappa}$. These results validate that the proposed method can preserve all motions in the other directions. The errors shown in Fig.

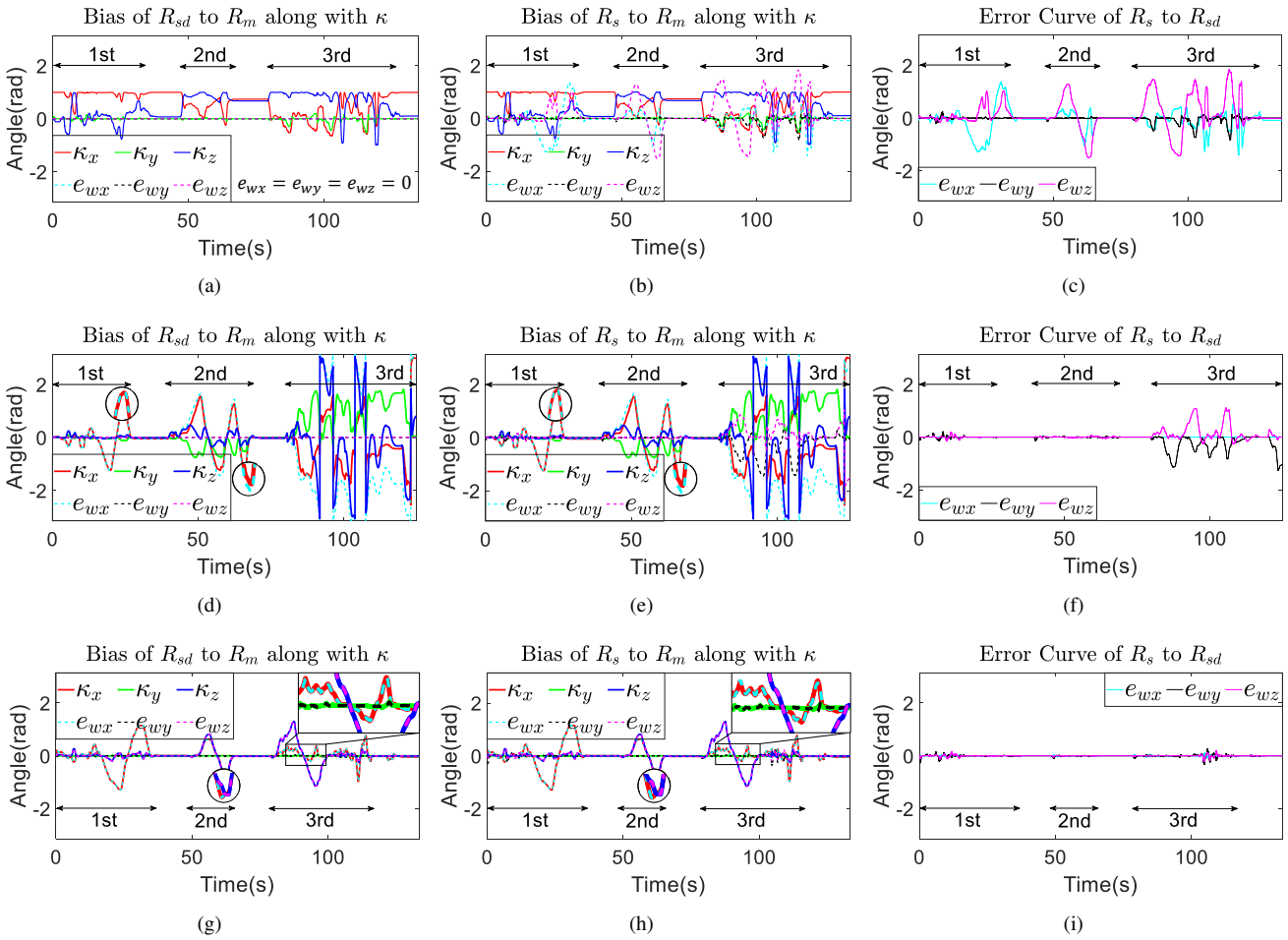


Fig. 9. The experimental results of the DMM, the EPDM, and our IOM method are presented in the first, second, and third row, respectively. $\boldsymbol{\kappa}$ has been scaled in (d), (e), (g), (h). Our method can avoid the unreachable orientation mappings for all the three configurations, which are marked in each figure.

9(i) are much smaller than those shown in Fig. 9(c)(f) for all the three configurations. These results demonstrate that the proposed method can avoid the unreachable mapping and generate more predictable, and safer robot motions.

## VII. Conclusion

To address a new asymmetrical teleoperation system with one DoF asymmetry, we proposed the perpendicular curve in $SO\left(3\right)$ and a perpendicular curve-based IOM approach. By decomposing the rotational motion into two orthogonal subspaces: the one along the geodesic curve $\gamma_{R_m,\boldsymbol{\kappa}}\left(\theta\right)$ and the other one along its perpendicular curve $\gamma_{\perp}$, the proposed method can only discard the rotation around the missing DoF $\boldsymbol{\kappa}$ and preserve the bias part along the perpendicular curve. The experiments demonstrated that the proposed method can avoid the unreachable orientation mappings, while preserving the remaining rotations. By using the proposed method, the unintentional orientations can be always detected and corrected. Therefore, the guidance actions can be modulated to any desirable level of haptic impedance within the performance capabilities of the master device. In the future work, the haptic rendering algorithm will be integrated with a passivity layer in the control framework to provide stable and transparent haptic feedback information about the missing DoF.

## Appendix

According to the definition of the exponential mapping (Rodrigues' formula), we have:

$$\begin{aligned}
&tr\left(\exp^{T}\left(\boldsymbol{\omega}_i\right)\exp\left(\theta\boldsymbol{\kappa}\right)\right)\\
&\quad= tr\left(I\right)+\frac{\sin\left\|\boldsymbol{\omega}_i\right\|}{\left\|\boldsymbol{\omega}_i\right\|}tr\left(\hat{\boldsymbol{\omega}}_i^{T}\right)+\frac{1-\cos\left\|\boldsymbol{\omega}_i\right\|}{\left\|\boldsymbol{\omega}_i\right\|^{2}}tr\left(\hat{\boldsymbol{\omega}}_i^{2}\right)\\
&\qquad+\sin\theta tr\left(\hat{\boldsymbol{\kappa}}\right)+\frac{\sin\left\|\boldsymbol{\omega}_i\right\|\sin\theta}{\left\|\boldsymbol{\omega}_i\right\|}tr\left(\hat{\boldsymbol{\omega}}_i^{T}\hat{\boldsymbol{\kappa}}\right)\\
&\qquad+\frac{\left(1-\cos\left\|\boldsymbol{\omega}_i\right\|\right)\sin\theta}{\left\|\boldsymbol{\omega}_i\right\|^{2}}tr\left(\hat{\boldsymbol{\omega}}_i^{2}\hat{\boldsymbol{\kappa}}\right)+\left(1-\cos\theta\right)tr\left(\hat{\boldsymbol{\kappa}}^{2}\right)\\
&\qquad+\frac{\sin\left\|\boldsymbol{\omega}_i\right\|\left(1-\cos\theta\right)}{\left\|\boldsymbol{\omega}_i\right\|}tr\left(\hat{\boldsymbol{\omega}}_i^{T}\hat{\boldsymbol{\kappa}}^{2}\right)\\
&\qquad+\frac{\left(1-\cos\left\|\boldsymbol{\omega}_i\right\|\right)\left(1-\cos\theta\right)}{\left\|\boldsymbol{\omega}_i\right\|^{2}}tr\left(\hat{\boldsymbol{\omega}}_i^{2}\hat{\boldsymbol{\kappa}}^{2}\right),
\end{aligned}\tag{33}$$

where $i=1,2$, $\hat{\boldsymbol{\omega}}_i$ and $\hat{\boldsymbol{\kappa}}$ represent the skew-symmetric matrix of $\boldsymbol{\omega}_i$ and $\boldsymbol{\kappa}$.

Denote $\boldsymbol{\omega}_1 = [x_1, y_1, z_1]^T$, $\boldsymbol{\omega}_2 = [x_2, y_2, z_2]^T$, $\boldsymbol{\kappa} = [x, y, z]^T$, we have:

$$\begin{aligned} x^2 + y^2 + z^2 = 1, \quad x_2 = 2kx - x_1, \\ y_2 = 2ky - y_1, \quad z_2 = 2kz - z_1, \\ x_1^2 + y_1^2 + z_1^2 = x_2^2 + y_2^2 + z_2^2, \end{aligned} \tag{34}$$

where $k = xx_1 + yy_1 + zz_1$.

By doing some algebraic calculations, it is easy to verify:

$$tr\left(\hat{\boldsymbol{\omega}}_1^T\right) - tr\left(\hat{\boldsymbol{\omega}}_2^T\right) = 0, \tag{35}$$

$$tr\left(\hat{\boldsymbol{\omega}}_1^2\right) - tr\left(\hat{\boldsymbol{\omega}}_2^2\right) = 0, \tag{36}$$

$$tr\left(\hat{\boldsymbol{\omega}}_1^T\hat{\boldsymbol{\kappa}}\right) - tr\left(\hat{\boldsymbol{\omega}}_2^T\hat{\boldsymbol{\kappa}}\right) = 0, \tag{37}$$

$$tr\left(\hat{\boldsymbol{\omega}}_1^2\hat{\boldsymbol{\kappa}}\right) - tr\left(\hat{\boldsymbol{\omega}}_2^2\hat{\boldsymbol{\kappa}}\right) = 0, \tag{38}$$

$$tr\left(\hat{\boldsymbol{\omega}}_1^T\hat{\boldsymbol{\kappa}}^2\right) - tr\left(\hat{\boldsymbol{\omega}}_2^T\hat{\boldsymbol{\kappa}}^2\right) = 0, \tag{39}$$

$$tr\left(\hat{\boldsymbol{\omega}}_1^2\hat{\boldsymbol{\kappa}}^2\right) - tr\left(\hat{\boldsymbol{\omega}}_2^2\hat{\boldsymbol{\kappa}}^2\right) = 0. \tag{40}$$

Thus, we have:

$$d_{\angle}\left(\exp\left(\boldsymbol{\omega}_1\right), \exp\left(\theta\boldsymbol{\kappa}\right)\right) = d_{\angle}\left(\exp\left(\boldsymbol{\omega}_2\right), \exp\left(\theta\boldsymbol{\kappa}\right)\right) \tag{41}$$

## REFERENCES


[1] P. F. Hokayem and M. W. Spong. Bilateral teleoperation: An historical survey. *Automatica*, 42(12):2035–2057, 2006.

[2] G. Niemeyer, C. Preusche, S. Stramigioli, and D. Lee. Telerobotics. In B. Siciliano and O. Khatib, editors, *Springer Handbook of Robotics, 2nd Edition*.

[3] A. Khasawneh, H. Rogers, J. Bertrand, K. C. Madathil, and A. Gramopadhye. Human adaptation to latency in teleoperated multi-robot human-agent search and rescue teams. *Automation in Construction*, 99:265–277, 2019.

[4] P. Malysz and S. Sirouspour. Teleoperating robots from the international space station: Microgravity effects on performance with force feedback. In *IEEE/RSJ Internation Conference on Intelligent Robots and Systems, Macau, China*, pages 8138–8144, Nov 2019.

[5] R. Miyazaki, K. Hirose, Y. Ishikawa, T. Kanno, and K. Kawashima. A master-slave integrated surgical robot with active motion transformation using wrist axis. *IEEE/ASME Transactions on Mechatronics*, 23(3):1215–1225, 2018.

[6] K. H.-Zaad and S. E. Salcudean. Analysis of control architectures for teleoperation systems with impedance/admittance master and slave manipulators. *The International Journal of Robotics Research*, 20(6):419–445, 2001.

[7] Y. Yuan, Y. Wang, and L. Guo. Force reflecting control for bilateral teleoperation system under time-varying delays. *IEEE Transactions on Industrial Informatics*, 15(2):1162–1172, 2019.

[8] P. Malysz. *A Kinematic Control Framework for Asymmetric Semi-autonomous Teleoperation Systems*. PhD thesis, McMaster University, 2012.

[9] P. Malysz and S. Sirouspour. Dual-master teleoperation control of kinematically redundant robotic slave manipulators. In *IEEE/RSJ Internation Conference on Intelligent Robots and Systems, St. Louis, MO, USA*, pages 5115–5120, Oct 2009.

[10] P. Malysz and S. Sirouspour. Trilateral teleoperation control of kinematically redundant robotic manipulators. *The International Journal of Robotics Research*, 30(13):1643–1664, 2011.

[11] P. Malysz and S. Sirouspour. A kinematic control framework for single-slave asymmetric teleoperation systems. *IEEE Transactions on Robotics*, 27(5):901–917, 2011.

[12] K. Razi and K. H.-Zaad. Analysis of coupled stability in multilateral dual-user teleoperation systems. *IEEE Transactions on Robotics*, 30(3):631–641, 2014.

[13] H. A. Talebi M. Shahbazi, S. F. Atashzar and R. V. Patel. Novel cooperative teleoperation framework: Multi-master/single-slave system. *IEEE Transactions on Mechatronics*, 20(4):1668–1679, 2015.

[14] P. Malysz and S. Sirouspour. Maneuverability and grasping experiments in teleoperation of nonholonomic/twin-armed robots. In *IEEE Haptics Symposium, Vancouver, BC, Canada*, pages 203–209, March 2012.

[15] P. Malysz and S. Sirouspour. Task performance evaluation of asymmetric semiautonomous teleoperation of mobile twin-arm robotic manipulators. *IEEE Transactions on Haptics*, 6(4):484–495, 2013.

[16] Z. Li and C.-Y. Su. Neural-adaptive control of single-master-multiple-slaves teleoperation for coordinated multiple mobile manipulators with time-varying communication delays and input uncertainties. *IEEE Transactions on Neural Networks and Learning Systems*, 24(9):1400–1413, 2013.

[17] W. He Y. Yin R. Johansson Y. Li, K. Liu and K. Zhang. Bilateral teleoperation of multiple robots under scheduling communication. *IEEE Transactions on Control Systems Technology*, Early Access(0):1–15, 2019.

[18] P. Malysz and S. Sirouspour. Control Framework and Human Maneuverability Experiments for Teleoperation of a Kinematically Deficient Robot. In *Proceedings of the 1st International Conference on Applied Bionics and Biomechanics, Venice, Italy*, pages 384–391, Oct 2010.

[19] K. Y. Lui, H. Cho, C. Ha, and D. Lee. First-person View Semi-autonomous Teleoperation of Cooperative Wheeled Mobile Robots with Visuo-haptic Feedback. *The International Journal of Robotics Research*, 36(5-7):840–860, 2017.

[20] C. J. M. Heemskerk, H. Boessenkool, F. C. T. V. Helm, and D. A. Abbink. Haptic Assistance Improves Tele-Manipulation With Two Asymmetric Slaves. *IEEE Transactions on Haptics*, 12(2):141–153, 2019.

[21] C. Meeker, T. Rasmussen, and M. Ciocarlie. Intuitive Hand Teleoperation by Novice Operators Using a Continuous Teleoperation Subspace. In *IEEE International Conference on Robotics and Automation, Brisbane, Australia*, pages 5821–5827, May 2018.

[22] S. C. Jacobsen, J. E. Wood, and D. F. Knutti. The UTAH/M.I.T. Dextrous Hand: Work in Progress. *The International Journal of Robotics Research*, 3(4):21–50, 1984.

[23] T. Takaki and T. Omata. High-Performance Anthropomorphic Robot Hand With Grasping-Force-Magnification Mechanism. *IEEE/ASME Transactions on Mechatronics*, 16(3):583–591, June 2011.

[24] C. Meeker and M. Ciocarlie. EMG-Controlled Non-Anthropomorphic Hand Teleoperation Using a Continuous Teleoperation Subspace. In *IEEE International Conference on Robotics and Automation, Montreal, Canada*, pages 1576–1582, May 2019.

[25] G. Gioioso, G. Salvietti, M. Malvezzi, and D. Prattichizzo. An Object-Based Approach to Map Human Hand Synergies onto Robotic Hands with Dissimilar Kinematics. In *Robotics: Science and Systems, Sydney, Australia*, pages 97–104, May 2012.

[26] G. Gioioso, G. Salvietti, M. Malvezzi, and D. Prattichizzo. Mapping Synergies From Human to Robotic Hands With Dissimilar Kinematics: An Approach in the Object Domain. *IEEE Transactions on Robotics*, 29(4):825–837, Aug 2013.

[27] A. Brygo, I. Sarakoglou, A. Ajoudani, N. G. Hernandez, G. Grioli, M. Catalano, D. G. Caldwell, and N. Tsagarakis. Synergy-Based Interface for Bilateral Tele-manipulations of a Master-Slave System with Large Asymmetries. In *IEEE International Conference on Robotics and Automation, Stockholm, Sweden*, pages 4859–4865, May 2016.

[28] A. Brygo, I. Sarakoglou, G. Grioll, and N. Tsagarakis. Synergy-Based Bilateral Port: A Universal Control Module for Tele-Manipulation Frameworks Using Asymmetric Master-Slave Systems. *Frontiers in Bioengineering and Biotechnology*, 5(1):1–18, 2017.

[29] G. Salvietti, L. Meli, G. Gioioso, M. Malvezzi, and D. Prattichizzo. Multicontact Bilateral Telemanipulation With Kinematic Asymmetries. *IEEE/ASME Transactions on Mechatronics*, 22(1):445–456, 2017.

[30] R. I. Hartley, J. Trumpf, Y. Dai, and H. Li. Rotation Averaging. *International Journal of Computer Vision*, 103(3):267–305, 2013.

[31] R. Hartley, J. Trumpf, and Y. Dai. Rotation Averaging and Weak Convexity. In *Proceeding of the 19th International Symposium on Mathematical Thoey of Networks and Systems*, pages 2435–2442, 2010.

[32] G. Li, D. Song, S. Xu, L. Sun, and J. Liu. Kinematic-free Orientation Control for a Deformable Manipulator Based on the Geodesic in Rotation Group SO(3). *IEEE Robotics and Automation Letters*, 3(3):2432–2438, 2018.

[33] L. Žlajpah. On Orientation Control of Functional Redundant Robots. In *IEEE Conference on Robotic and Automation, Singapore*, pages 2475–2482, 2017.